

UC Berkeley

UC Berkeley Previously Published Works

Title

Spherical trihedral metallo-borosphenenes

Permalink

<https://escholarship.org/uc/item/59z4w76k>

Journal

Nature Communications, 11(1)

ISSN

2041-1723

Authors

Chen, Teng-Teng

Li, Wan-Lu

Chen, Wei-Jia

et al.

Publication Date

2020-06-01

DOI








10.1038/s41467-020-16532-x

Copyright Information

This work is made available under the terms of a Creative Commons Attribution License, available at <https://creativecommons.org/licenses/by/4.0/>

Peer reviewed

Spherical trihedral metallo-borospherenes

Teng-Teng Chen ^{1,5}, Wan-Lu Li^{2,5} , Wei-Jia Chen¹, Xiao-Hu Yu ³, Xin-Ran Dong⁴, Jun Li ^{2,4}  & Lai-Sheng Wang ¹ 

The discovery of borospherenes unveiled the capacity of boron to form fullerene-like cage structures. While fullerenes are known to entrap metal atoms to form endohedral metallofullerenes, few metal atoms have been observed to be part of the fullerene cages. Here we report the observation of a class of remarkable metallo-borospherenes, where metal atoms are integral parts of the cage surface. We have produced $\text{La}_3\text{B}_{18}^-$ and $\text{Tb}_3\text{B}_{18}^-$ and probed their structures and bonding using photoelectron spectroscopy and theoretical calculations. Global minimum searches revealed that the most stable structures of $\text{Ln}_3\text{B}_{18}^-$ are hollow cages with D_{3h} symmetry. The B_{18} -framework in the $\text{Ln}_3\text{B}_{18}^-$ cages can be viewed as consisting of two triangular B_6 motifs connected by three B_2 units, forming three shared B_{10} rings which are coordinated to the three Ln atoms on the cage surface. These metallo-borospherenes represent a new class of unusual geometry that has not been observed in chemistry heretofore.

¹Department of Chemistry, Brown University, Providence, RI 02912, USA. ²Department of Chemistry and Key Laboratory of Organic Optoelectronics & Molecular Engineering of Ministry of Education, Tsinghua University, 100084 Beijing, China. ³Institute of Theoretical and Computational Chemistry, Shaanxi Key Laboratory of Catalysis, School of Chemical & Environment Sciences, Shaanxi University of Technology, 723000 Hanzhong, China. ⁴Department of Chemistry, Southern University of Science and Technology, 518055 Shenzhen, China. ⁵These authors contributed equally: Teng-Teng Chen, Wan-Lu Li. email: wanyluli0716@gmail.com; junli@tsinghua.edu.cn; lai-sheng_wang@brown.edu

The electron deficiency of boron often leads to electron delocalization and the violation of the octet rule in boron compounds and three-dimensional (3D) cage units in different bulk boron allotropes^{1–3}. Because of the strong boron–boron bonding, there were speculations about the formation of boron nanotubes composed of a triangular boron lattice^{4,5}, after the discovery of carbon nanotubes. The triangular boron lattice can be viewed as a graphene-like sheet with the filling of a boron atom in each B₆ hexagon. Further theoretical calculations revealed, however, that triangular lattices with hexagonal vacancies were more stable and more suitable to construct boron nanotubes^{6,7}. In the meantime, combined spectroscopic and theoretical studies have shown that size-selected boron clusters all have 2D structures with delocalized multi-center bonding within the cluster plane^{8–11}. The discovery of the hexagonal 2D B₃₆ clusters provided the first experimental evidence of the viability of atom-thin boron nanostructures with hexagonal vacancies, named as borophene akin to graphene¹². Borophenes have been recently synthesized using atomic vapor deposition on Ag(111) substrates^{13,14}, forming a new class of synthetic 2D nanomaterials¹⁵. The analogy between nanostructures made of boron and carbon has been further extended when the B₄₀ and B₃₉[−] clusters were found to have global minimum cage structures^{16,17}, i.e. borospherenes analogous to the fullerenes. Fullerenes are known to form endohedral metallofullerenes for alkali, alkali earth, lanthanide, and actinide elements^{18,19}, albeit not for transition metals. Heterofullerenes in which one carbon atom is substituted by a transition metal atom have been observed in the gas phase, but the metal substitution induces large local structural distortions and such heterofullerenes have not been synthesized in the bulk^{20–22}. The first cage cluster made of multiple metal atoms and carbons was proposed to be Ti₈C₁₂⁺ (metallo-carbohedrene)²³. However, subsequent theoretical calculations showed that the metallo-carbohedrene is not stable and the global minimum of Ti₈C₁₂⁺ consisted of a tetrahedral, close-packed Ti₈ clusters coordinated by six C₂ units on the cluster surface²⁴. In the present article, we report the first observation of a class of metallo-borospherenes, hollow cage clusters consisting of three lanthanide (Ln) atoms and 18 boron atoms (Ln₃B₁₈[−]).

Transition-metal-doped boron clusters were first found to form aromatic borometallic molecular wheels, M@B_n[−] (*n* = 8–10)^{25,26}, as well as metal-centered nanotubular structures²⁷. More interestingly, it has been shown that transition metals can be an integral part of larger 2D boron clusters²⁸, leading to the possibility of metallo-borophenes²⁹. Lanthanide-doped boron clusters, however, have been found recently to form very different structures, due to both charge transfer interactions and strong (*d*–*p*) π bonding³⁰. For example, lanthanide-doped boron clusters do not form similar borometallic molecular wheels as the transition metals. Instead, they form inverse-sandwich-type structures for Ln₂B_{*n*}[−] clusters (*n* = 7–9)^{31,32}. The most recent study indicates that the inverse-sandwich structure may extend to form lanthanide-boron nanowires³³.

Here we report a joint photoelectron spectroscopy (PES) and quantum chemistry study of two tri-lanthanide-doped B₁₈ clusters (La₃B₁₈[−] and Tb₃B₁₈[−]), which are found to possess unprecedented *D*_{3h} cage structures with the Ln atoms being integral parts of the cage surface. These *D*_{3h} metallo-borospherenes belong to an unusual class of geometry known as spherical trihedron. The B₁₈ framework consists of two B₆ triangles connected by three B₂ units, forming three shared B₁₀ rings. The high stability of the spherical trihedral structures is derived from the strong interactions between the Ln atoms and the B₁₀ rings via charge transfer interactions and *d*–*p* covalent bonding. Theoretical calculations show that the entire series of lanthanide elements (Ln = La–Lu) can form spherical trihedral Ln₃B₁₈[−]

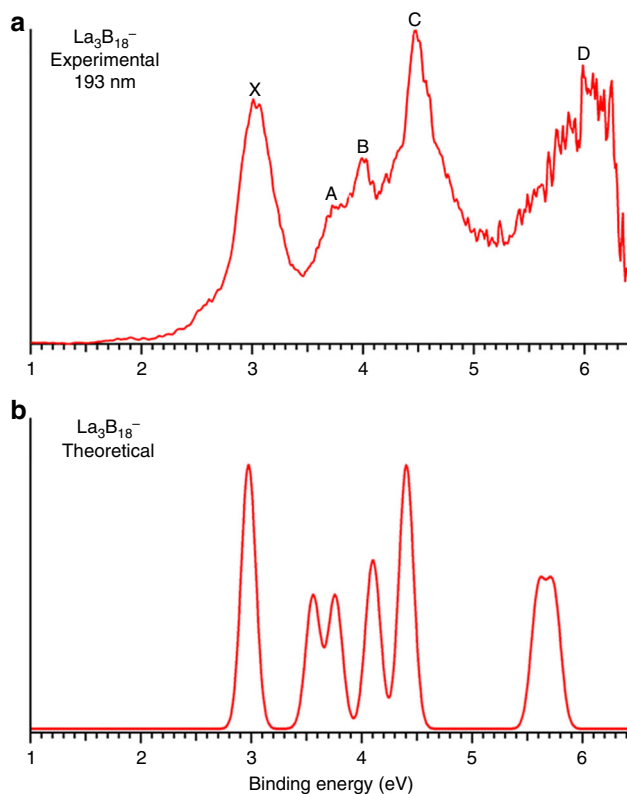


Fig. 1 Photoelectron spectrum of La₃B₁₈[−]. **a** At 193 nm. **b** The simulated spectrum.

metallo-borospherenes with tunable magnetic properties, making them a fascinating series of building blocks for new types of magnetic materials.

Results and discussion

Photoelectron spectroscopy. The PE spectrum at 193 nm was first measured for the La₃B₁₈[−] cluster (Fig. 1a), which was found to exhibit a relatively simple pattern compared with that of the recently reported La₃B₁₄[−] cluster³³. This observation suggested that La₃B₁₈[−] should possess a highly symmetric structure. Subsequently, we also obtained the spectrum of a late-Ln cluster Tb₃B₁₈[−] (Fig. 2a) and observed a spectral pattern, exhibiting some similarities to that of La₃B₁₈[−] and suggesting that these two Ln-doped boron clusters should have similar structures and chemical bonding. The well-resolved PES features of the Ln₃B₁₈[−] clusters serve as electronic fingerprints to allow analyses of their structures and chemical bonding by comparing with theoretical calculations, as shown in Figs. 1b, 2b, and Supplementary Tables S1 and S2 for Ln = La and Tb, respectively.

The spectrum of La₃B₁₈[−] displayed five well-resolved bands labeled as X, A, B, C, and D (Fig. 1a). The X band yielded the first vertical detachment energy (VDE) of 2.97 eV for La₃B₁₈[−]. The adiabatic detachment energy (ADE) for band X was evaluated from its onset to be 2.80 eV, which also represents the electron affinity (EA) of neutral La₃B₁₈. The higher binding energy bands (A, B, C, and D) correspond to detachment transitions to the excited states of neutral La₃B₁₈. The A band at 3.64 eV was broad and not well resolved at 193 nm, but it was slightly better resolved in the 266 nm spectrum (Supplementary Fig. 1). This broad spectral feature could be due to geometry changes upon electron detachment or overlapping detachment transitions. Band B at 4.01 eV is sharper compared with band A (Fig. 1a). An intense and sharp band C at 4.43 eV was clearly resolved in the 193 nm

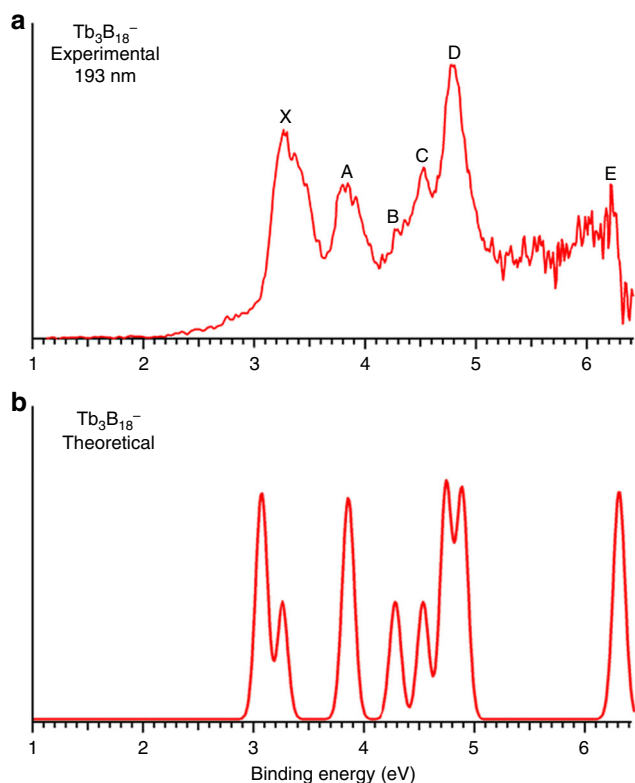


Fig. 2 Photoelectron spectrum of $\text{Tb}_3\text{B}_{18}^-$. **a** At 193 nm. **b** The simulated spectrum.

spectrum. Following a large energy gap, a broad band (D) was observed above ~ 5.5 eV. Due to the poor signal-to-noise ratio, band D was tentatively assigned for the sake of discussion.

The PE spectrum of $\text{Tb}_3\text{B}_{18}^-$ showed five well-resolved peaks assigned as X, A, B, C, D (Fig. 2a). The X band gave rise to a VDE of 3.26 eV for $\text{Tb}_3\text{B}_{18}^-$ and an ADE of 3.13 eV, which is also the EA of neutral Tb_3B_{18} . Band A was observed at a VDE of 3.84 eV, followed by three closely-lying bands (B, C, D). Band B at 4.28 eV and band C at 4.52 eV were relatively weak and closely spaced, whereas band D at 4.77 eV was much more intense. Beyond ~ 5 eV, the signal-to-noise ratio was poor and no obvious spectral bands were observed. Band E close to the threshold at a VDE of ~ 6.2 eV was tentatively labeled. The overall spectral pattern for $\text{Tb}_3\text{B}_{18}^-$ exhibits some similarity to that of $\text{La}_3\text{B}_{18}^-$. In particular, the strong X and D bands in $\text{Tb}_3\text{B}_{18}^-$ are similar to the strong X and C bands in $\text{La}_3\text{B}_{18}^-$. There is a large energy gap on the high binding energy side in both spectra. Similar spectral patterns could be an indication of similar structures, as have been observed for a series of dilanthanide clusters (Ln_2B_8^-)³¹.

Global minimum structural searches. The low-lying isomers within 55 kcal mol⁻¹ of the global minimum at the levels of PBE/TZP and PBE0/TZP are presented in Supplementary Fig. 2. The global minimum of $\text{La}_3\text{B}_{18}^-$ is a hollow cage with a closed-shell ground state (1A_1) and D_{3h} symmetry. This is a hetero-metallo-borospherene, in which the three La atoms are integral parts of the cage surface, as shown in Fig. 3. All the other low-lying isomers are low-symmetry 3D structures, many of which are distorted cages. The highly symmetric global minimum D_{3h} metallo-borospherene exhibits overwhelming stability relative to the other low-lying isomers: it is more stable than the nearest isomer with C_s symmetry by ~ 19 kcal mol⁻¹ at the PBE/TZP and PBE0/TZP levels of theory. The B_{18} framework in the $\text{La}_3\text{B}_{18}^-$ cage can be viewed as consisting of two B_6 triangles linked together at their

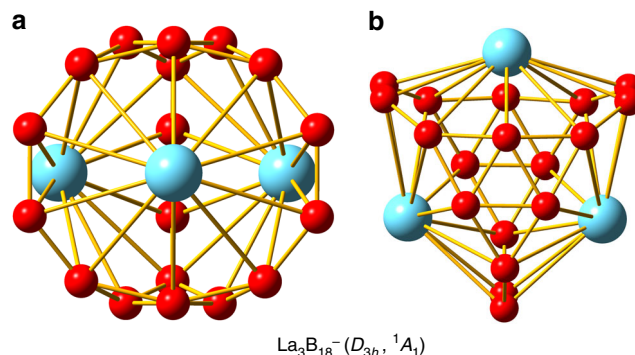


Fig. 3 The global minimum structure of $\text{La}_3\text{B}_{18}^- (D_{3h}, ^1A_1)$ at the PBE0/TZP level. **a** The C_3 axis is along the page vertically. **b** The C_3 axis is perpendicular to the page.

three corners by three B_2 units, creating three shared B_{10} rings along the C_3 axis. The three La atoms are coordinated by the three B_{10} rings, giving rise to the closed cage structure. The $\text{La}_3\text{B}_{18}^-$ metallo-borospherene has an oblate shape with a diameter of 4.62 Å along the C_3 axis (between the two B_6 triangles) and 5.09 Å encompassed by the three equatorial La atoms. The relevant bond lengths of the $\text{La}_3\text{B}_{18}^-$ metallo-borospherene are shown in Supplementary Fig. 3a.

The hollow cage structure of $\text{La}_3\text{B}_{18}^-$ was totally unexpected and the geometry is highly unusual. To further examine its stability and robustness, we performed ab initio molecular dynamics (AIMD) simulations at different temperatures, 300, 500, 700, and 1000 K (see Supplementary Fig. 4). We found that even at 1000 K the $\text{La}_3\text{B}_{18}^-$ metallo-borospherene is dynamically stable for the 13 ps duration of the simulations. At 1000 K, the structure displayed a root-mean-square-deviation of 0.199 Å and a maximum bond length deviation of 0.260 Å during the simulations.

The similarity in their PE spectra suggested that the global minima of $\text{Tb}_3\text{B}_{18}^-$ and $\text{La}_3\text{B}_{18}^-$ should be similar. Because of the localized and nonbonding nature of the 4f orbitals in Tb, we optimized the D_{3h} structure for $\text{Tb}_3\text{B}_{18}^-$ using the 4f-in-core pseudopotential³⁴. The structural parameters of the $\text{Tb}_3\text{B}_{18}^-$ metallo-borospherene are similar to those for $\text{La}_3\text{B}_{18}^-$ (Supplementary Fig. 3), except that the Tb–B and B–B bond lengths are all slightly shorter due to the smaller atomic radius of Tb as a result of the lanthanide contraction. Because of the use of the 4f-in-core pseudopotential, the spin state of the $\text{Tb}_3\text{B}_{18}^-$ metallo-borospherene was not determined from the geometry optimization. We performed broken symmetry calculations and compared the relative energies between the ferromagnetic and antiferromagnetic couplings of the 4f electrons, as shown in Supplementary Table 3 for $\text{Tb}_3\text{B}_{18}^-$, as well as for $\text{Pr}_3\text{B}_{18}^-$. The relative energies due to the inter-atomic spin couplings of the unpaired 4f electrons are relatively small, although the high spin ferromagnetic coupling seems to give the lowest energy in both cases. Hence, the spin multiplicity of the $\text{Tb}_3\text{B}_{18}^-$ metallo-borospherene should be 19 (with 18 unpaired 4f electrons).

Comparison between the experimental and theoretical results.

To validate the D_{3h} cage structure for $\text{La}_3\text{B}_{18}^-$ and $\text{Tb}_3\text{B}_{18}^-$, we calculated their ADEs and VDEs using the $\Delta\text{SCF-TDDFT}$ formalism. Figures 1b, 2b present the simulated spectra for the D_{3h} global minimum structures, in comparison with the experimental data. The computed ADE/VDE₁ at the CCSD(T) level are 2.828/2.972 eV for $\text{La}_3\text{B}_{18}^-$ (Supplementary Table 4), in excellent agreement with the experimental data of 2.80/2.97 eV. As shown in Fig. 4, the valence MOs of $\text{La}_3\text{B}_{18}^-$ are mainly of La-B d-p and

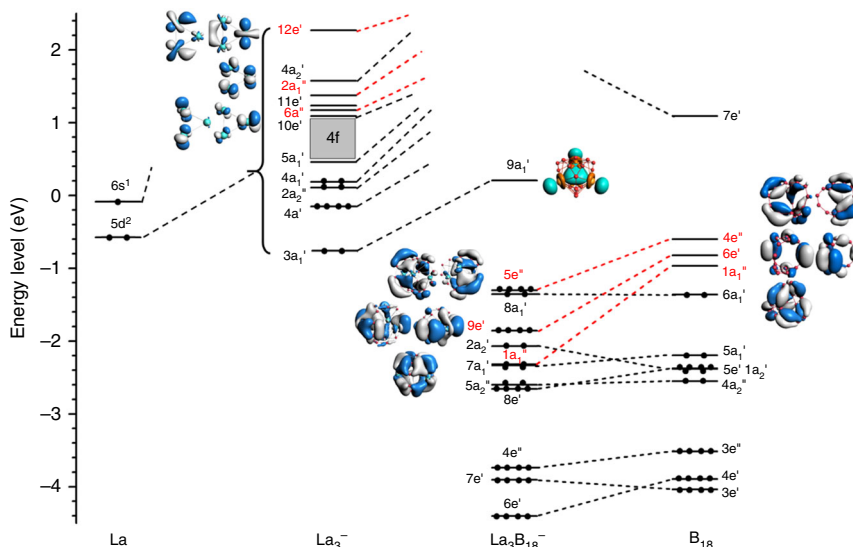


Fig. 4 The Kahn-Sham molecular orbital correlation diagram for $\text{La}_3\text{B}_{18}^-$ (D_{3h} , $1A_1$). It shows the interactions between the 5d orbitals of the three La atoms and the group orbitals of the B_{18} moiety.

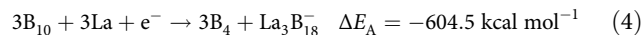
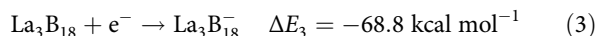
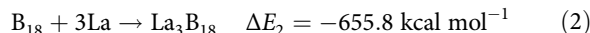
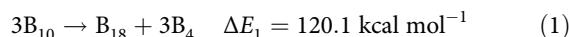
B *sp* characters. Because $\text{La}_3\text{B}_{18}^-$ has a closed-shell configuration, single-electron removal from each molecular orbital (MO) yields one detachment channel, as shown in Supplementary Table 1. The computed VDEs for detachment from the $5e''$ HOMO (2.972 eV) and $8a_1'$ HOMO-1 (2.987 eV) are very close to each other, in excellent agreement with the experimental VDE of the X band (2.97 eV). In fact, each of the observed PES band corresponds to two detachment channels, as given in Supplementary Table 1, where the electron configurations and final state symmetries are also presented. The simulated spectral patterns and the experimental spectra are in excellent agreement, providing considerable credence for the D_{3h} cage global minimum for $\text{La}_3\text{B}_{18}^-$. We have also simulated the PE spectra for the next nine higher-lying isomers of $\text{La}_3\text{B}_{18}^-$, as shown in Supplementary Fig. 5. None of these spectra fits the experimental spectrum, giving additional support for the D_{3h} global minimum structure.

The computed ADE/VDE for $\text{Tb}_3\text{B}_{18}^-$ are 2.901/3.017 eV at the CCSD(T) level (Supplementary Table 4), slightly underestimated relative to the experimental data of 3.13/3.26 eV probably due to the use of the 4*f*-in-core approximation as well as the incomplete account of electron correlations. Nevertheless, the theoretical results by not considering the 4*f* electrons and detachment channels are still in very good agreement with the experimental data, as can be seen in Fig. 2 and Supplementary Table 2. These results are consistent with our previous observations that the detachment cross sections of the 4*f* electrons are much weaker and the PE spectra of Ln–B binary clusters are dominated by the Ln–B *d*–*p* and B *sp* detachment channels^{31,32}.

Stabilities of the first metallo-borospherenes. The observation of the $\text{La}_3\text{B}_{18}^-$ and $\text{Tb}_3\text{B}_{18}^-$ cage clusters, in which the three Ln atoms are integral parts of the cage surface, is unprecedented. The two B_6 triangles in the D_{3h} structure are reminiscent of the B_{40} borospherene¹⁶, which consists of eight fused B_6 triangles on a spherical surface. Hence, the $\text{Ln}_3\text{B}_{18}^-$ cage clusters can be viewed as a new class of metallo-borospherenes. Networked metallo-fullerenes usually involve a single transition-metal atom substituting one carbon atom on the fullerene surface^{20–22}. The incorporation of multiple metal atoms on the borospherene surface is due to the flexibility of the 2D boron network, which is a direct result of the electron deficiency of boron. It is interesting to note that the crystal structure of a Ni–Zn boride ($\text{Ni}_{21}\text{Zn}_2\text{B}_{24}$)

was shown to contain characteristic cages of B_{20} units, with an octahedral Ni_6 cluster nested inside³⁵. Our observation of the $\text{Ln}_3\text{B}_{18}^-$ metallo-borospherenes represents the first isolated molecules of Ln–B cages in the gas phase.

To understand the stability of these remarkable cage structures, we carried out fragment MO analyses by first considering the construction of the B_{18} framework in two different pathways and then its bonding with the three La atoms, as schematically shown in Fig. 5. Figure 5a shows one possible path to construct the B_{18} framework by the fusion of three B_{10} rings. Four of the boron atoms in each B_{10} ring are shared with the other B_{10} rings, which each coordinate to a La atom to form three shared $\text{La}@\text{B}_{10}$ units. This hypothetical formation pathway of $\text{La}_3\text{B}_{18}^-$ can be expressed by the following steps:



The energetics were calculated from single-point energy differences of the reactants and products, using the geometries directly taken from the optimized $\text{La}_3\text{B}_{18}^-$ cage at the PBE/TZP level of theory. The interactions between the B_{18} framework and the three La atoms are extremely strong (steps 2 and 3), which underlies the stability of the $\text{La}_3\text{B}_{18}^-$ cage. It should be noted that in platonic solids four surfaces are the minimum number to form a 3D object, i.e., the tetrahedron. However, Fig. 5a shows that three $\text{La}@\text{B}_{10}$ surfaces are fused together to form the D_{3h} $\text{La}_3\text{B}_{18}^-$ cage. This is because the $\text{La}@\text{B}_{10}$ surface is curved. It turns out that the $\text{Ln}_3\text{B}_{18}^-$ metallo-borospherenes belong to a class of geometry mathematically known as *n*-gonal hosohedron, which is basically a tessellation of lunes on a spherical surface, such that each lune shares the same two vertices. Thus, the D_{3h} $\text{La}_3\text{B}_{18}^-$ cage is a trigonal hosohedron, also known as spherical trihedron, where the two vertices consist of the triangular B_6 units. To the best of our knowledge, such a geometry has not been observed in any cluster or molecular systems heretofore.

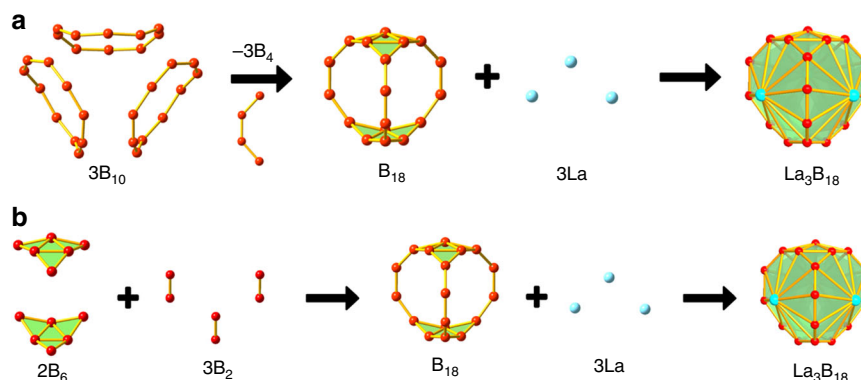
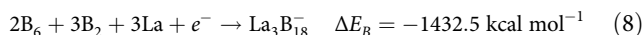
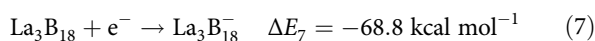
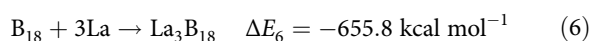
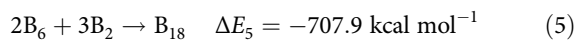


Fig. 5 Schematic pathways for the formation of the D_{3h} $\text{Ln}_3\text{B}_{18}^-$ metallo-borospherenes. Two pathways for the construction of the B_{18} framework and its bonding with the three Ln atoms are depicted. **a** The fused B_{10} ring pathway. **b** The B_2 -linked triangular B_6 pathway.

Figure 5b shows another pathway to construct the $\text{La}_3\text{B}_{18}^-$ cage, in which the B_{18} framework is formed by two triangular B_6 motifs linked by three B_2 bridges, such that three B_{10} rings are created. This hypothetical pathway can be represented by the following steps:



The interactions between the B_{18} framework and the three La atoms to form the $\text{La}_3\text{B}_{18}^-$ cage are represented by steps 2/3 or 6/7 with an estimated binding energy of $724.6 \text{ kcal mol}^{-1}$, i.e., $241.5 \text{ kcal mol}^{-1}$ for the binding energy between each La atom and the B_{10} ring. This huge La- B_{10} binding energy underlies the extraordinary stability of the $\text{La}_3\text{B}_{18}^-$ metallo-borospherene. Compared with the pathway in Fig. 5a, the pathway in Fig. 5b is more favorable energetically since each step is exothermic. We should emphasize, though, that these exercises provide different views of the unprecedented hollow cage structures. The two pathways to construct the $\text{La}_3\text{B}_{18}^-$ cage depicted in Fig. 5 certainly do not represent the mechanisms about how it is formed.

The nature of the bonding between B_{18} and the La atoms. Since the global minimum of B_{18} is a planar structure³⁶, the stabilization of the 3D B_{18} framework is entirely due to its strong bonding with the three La atoms, as discussed above. We have analyzed the nature of the La- B_{10} bonding in the $\text{La}_3\text{B}_{18}^-$ metallo-borospherene using several different methods. The MO energy-level diagram and the relevant MOs of $\text{La}_3\text{B}_{18}^-$ derived from the La_3^- and B_{18} moieties are shown in Fig. 4. The $5e''$, $9e'$, and $1a_1''$ MOs of $\text{La}_3\text{B}_{18}^-$ (red-colored) represent the bonding orbitals between the three La atoms and the B_{18} moiety, mainly corresponding to the interactions between the irreducible representations, $4e''$, $6e'$, and $1a_1''$ on the B_{18} moiety and $6e''$, $12e'$, and $2a_1''$ on the La_3^- moiety (the red highlighted MOs). Supplementary Table S5 gives the compositions of the $5e''$, $9e'$, and $1a_1''$ MOs, which are dominated by contributions from the B_{18} moiety. Hence, there is a strong charge transfer from La to B_{18} , resulting in a closed-shell $\text{La}_3\text{B}_{18}^-$ with a large HOMO-LUMO gap of 1.51 eV computed at the PBE/TZP level. The La atoms are in their favorite +III oxidation state in $\text{La}_3\text{B}_{18}^-$, which can be viewed approximately as $(\text{La}^{3+})_3[\text{B}_{18}^{10-}]$. As shown in Fig. 4, the $6e''$, $12e'$, and $2a_1''$ irreducible representations on the La_3^- moiety are

of La $5d$ characters, while the $4e''$, $6e'$, and $1a_1''$ irreducible representations on the B_{18} framework are of B $2p$ characters. Hence, the $5e''$, $9e'$, and $1a_1''$ MOs also represent significant La $5d$ and B_{18} $2p$ covalent bonding. It is the strong covalent and ionic bonding between the La atoms and the B_{10} rings that gives rise to the extraordinary stability of the $\text{La}_3\text{B}_{18}^-$ cage structure. These bonding characteristics are found in all lanthanide boride compounds due to the low electronegativity of the lanthanide elements and their diffuse $5d$ orbitals³⁷.

The La- B_{10} interactions can be further characterized using the EDA-NOCV method with $\text{B}_{18} (\dots 6a_1'^2 1a_1''^0 6e''^0 4e''^0)$ and $\text{La}_3^- (\dots 6e''^4 2a_1''^2 12e'^4)$ fragments, a powerful energy decomposition tool to give insight into chemical bonding³⁸. We analyzed the $\text{B}_{18} \dots \text{La}_3^-$ interaction by the decomposition of the orbital terms into pairwise contributions, as shown in Supplementary Fig. 6. There are three major terms ΔE_1 , ΔE_2 , and ΔE_3 associated with the deformation densities $\Delta\rho_1$, $\Delta\rho_2$, and $\Delta\rho_3$, respectively. The remaining terms contribute <10% to the total orbital interactions. The color code of the deformation densities indicates the direction of the charge flow from red \rightarrow blue. It is interesting to see that the $1a_1''$ orbital of $\text{La}_3\text{B}_{18}^-$, which is analogous to the $(d-p)\delta$ bonding MO in the Ln_2B_8^- inverse sandwich complexes^{31,32}, contributes significantly (25.7% from the EDA-NOCV analyses, Supplementary Fig. 6) to the stability of the orbital interaction. The other two stronger $\Delta\rho_2$ (34.8%) and $\Delta\rho_3$ (28.9%) deformation densities correspond to the degenerate $9e'$ and $5e''$ MOs, respectively. The direction of the charge flow is from the La_3^- to the B_{18} moiety, consistent with the fragment MO analyses discussed above (Fig. 4).

We further analyzed the chemical bonding in the $\text{La}_3\text{B}_{18}^-$ metallo-borospherene using the adaptive natural density partitioning (AdNDP) approach³⁹, as shown in Fig. 6. The first row displays nine localized two-center two-electron ($2c-2e$) σ bonds formed within the three B_2 units and between the B_2 units and the three apexes of the two B_6 triangles. The second row reveals the delocalized bonds in the B_6 triangles, with four three-center two-electron ($3c-2e$) σ bonds within each B_6 unit. The multi-center $12c-2e$ and $18c-2e$ delocalized bonds can be viewed as π bonds within the B_6 units. The third row represents totally delocalized σ and π bonds within the B_{18} framework. The last row shows five totally delocalized $21c-2e$ bonds between the La atoms and the B_{18} framework, corresponding to the $5e''$, $9e'$, and $1a_1''$ MOs in Fig. 4. We also found that the $\text{La}_3\text{B}_{18}^-$ metallo-borospherene possesses both 3D aromaticity with calculated nucleus-independent chemical shifts (NICS)⁴⁰ of -47.87 ppm at the cage center, and planar aromaticity on each B_6 triangles with NICS(0) of -31.44 ppm and NICS(1) of -2.16 above the plane center, as shown in Supplementary Table 6, where the aromaticity in the



Fig. 6 Chemical bonding analyses of $\text{La}_3\text{B}_{18}^-$ ($D_{3h} \ ^1A_1$). The analyses were done using the AdNDP method²⁹. ON stands for occupation number.

metallo-borosphenere is compared with that of the recently synthesized cubic $[\text{Zn}^{\text{I}}]_8$ compound⁴¹.

We also performed bond-order index analyses for the B–B and La–B interactions, as presented in Supplementary Table 7. The B₂ bridges have shorter bond lengths and higher bond orders than those of the B₆ triangles. In terms of the La–B interactions, the distances and bond order indices are similar to those in the lanthanide–boron complexes reported previously^{30–33}.

A new class of spherical trihedron metallo-borospheneres. The discoveries of the $\text{La}_3\text{B}_{18}^-$ and $\text{Tb}_3\text{B}_{18}^-$ metallo-borospheneres suggest that other lanthanide elements could also form similar structures because of the similarity in the chemical properties of the whole series of lanthanides. We have calculated the D_{3h} cage structures for all the lanthanide elements, $\text{Ln}_3\text{B}_{18}^-$ (Ln = Ce–Lu). The coordinates obtained at the PBE0 level are given as Supplementary Data 1, whereas those of $\text{La}_3\text{B}_{18}^-$ and La_3B_{18} are provided in Supplementary Table 8. All these structures are indeed minima on their potential energy surfaces. Hence, we conclude that there indeed exist a whole class of $\text{Ln}_3\text{B}_{18}^-$ metallo-borospheneres. While borospheneres have not been observed beyond the B₄₀ cluster⁴², the unique bonding characteristics between lanthanide and boron suggest that other lanthanide metallo-borospheneres with different sizes and Ln_xB_y^- stoichiometries may exist. Recent studies of transition-metal borides showed that the metal–boron interactions have major influences on their magnetic properties^{43,44}. Hence, the understanding of Ln–B interactions in the metallo-borosphenere systems may provide insights for the design of lanthanide borides with tunable magnetic or catalytic properties.

In conclusion, we report the observation of the first tri-lanthanide-doped boron cage clusters (metallo-borospheneres), in which the metal atoms are integral parts of the cage surface. Photoelectron spectra of two representative systems, $\text{Ln}_3\text{B}_{18}^-$ (Ln = La, Tb), show similar and relatively simple spectral patterns,

suggesting that they have similar highly symmetric structures. Theoretical calculations reveal that the $\text{Ln}_3\text{B}_{18}^-$ anions have cage-like structures with D_{3h} symmetry: two planar B₆ triangular units linked by three B₂ bridges to form the B₁₈ framework consisting of three shared B₁₀ rings coordinated to the three Ln atoms. Strong ionic and covalent chemical bonding is found between the Ln atoms and the B₁₈ framework. The extraordinary stabilities of the metallo-borospheneres are understood by various theoretical analyses. $\text{La}_3\text{B}_{18}^-$ is found to have a closed-shell electron configuration with a large HOMO–LUMO gap and possesses 3D aromaticity. The $\text{Ln}_3\text{B}_{18}^-$ cage complexes are expected to exist for all lanthanide elements, suggesting the possibility that there may exist a large class of lanthanide metallo-borospheneres with different Ln/B stoichiometries and tunable properties.

Methods

Experimental details. The experiments were carried out using a magnetic-bottle PES apparatus equipped with a laser vaporization supersonic cluster source, details of which have been published elsewhere¹¹. The $\text{La}_3\text{B}_{18}^-$ and $\text{Tb}_3\text{B}_{18}^-$ clusters were produced by laser vaporization of a La/¹¹B or Tb/¹¹B mixed target, respectively. The laser-induced plasma was cooled by a He carrier gas seeded with 5% Ar, initiating nucleation between the boron and lanthanide atoms. The nascent clusters were entrained in the carrier gas and underwent a supersonic expansion. Negatively-charged clusters were extracted from the collimated cluster beam and analyzed by a time-of-flight mass spectrometer. Both pure (B_n[−]) and mixed (Ln_xB_y[−]) clusters were produced from the cluster source. The $\text{La}_3\text{B}_{18}^-$ and $\text{Tb}_3\text{B}_{18}^-$ clusters of current interest were mass-selected and photodetached by the 193 nm (6.424 eV) radiation from an ArF excimer laser or the fourth harmonics from a Nd:YAG laser (266 nm, 4.661 eV). Photoelectrons were collected and analyzed in a 3.5-m-long electron flight tube at nearly 100% efficiency. The photoelectron spectra were calibrated by the known transitions of Au[−] and Bi[−]. The resolution of the PES apparatus ($\Delta\text{KE}/\text{KE}$) was around 2.5%, that is, about 25 meV for photoelectrons with 1 eV kinetic energy (KE).

Computational methods. Unbiased global-minimum structural searches for the $\text{La}_3\text{B}_{18}^-$ cluster were performed using the TGMIn 2.0 code⁴⁵. The global minimum structure of $\text{Tb}_3\text{B}_{18}^-$ was not searched separately. More than 2000 structures were evaluated for $\text{La}_3\text{B}_{18}^-$ using the constrained Basin-Hopping algorithm at the PBE/DZP^{46,47} level from the ADF 2017 software⁴⁸. A D_{3h} cage structure was found to be

the global minimum, which was significantly lower in energy in comparison to the next lowest-lying isomer (Supplementary Fig. 2). To confirm the stability of the global minimum, we conducted another 500 structural searches, using the D_{3h} cage as the seed structure. No structures with lower energies were found. All the local minima were verified via harmonic vibrational frequency calculations. The frozen-core approximation was employed for the inner shells of $[1s^2]$ for B and $[1s^2-4d^{10}]$ for the La atoms. The zero-order regular approximation⁴⁹ was applied, to account for the scalar relativistic effects. Low-lying isomers were subsequently optimized using the PBE and PBE0 density functionals⁵⁰ along with the TZP basis sets. Born–Oppenheimer molecular dynamic simulations were further carried out on $\text{La}_3\text{B}_{18}^-$ for 13 ps using the CP2K code⁵¹ at different temperatures, from 300 to 1000 K (Supplementary Fig. 4). To minimize the 4f-electron induced complexity (i.e. spin multiplicity) and considering the negligible geometry change due to the occupations of the localized 4f orbitals (radial-density maximum probability radii $<0.5 \text{ \AA}$), we used the 4f-in-core pseudopotentials³⁴ for the lanthanide elements to optimize the geometric parameters in the other $\text{Ln}_3\text{B}_{18}^-$ (Ln = Ce–Lu) species.

The simulation of the PE spectra was done using the $\Delta\text{SCF-TDDFT}$ method⁵² with the SAOP exchange-correlation functional⁵³ to account for the long-range interactions. The ground state adiabatic and vertical detachment energies were calculated at the DFT levels, as well as the more accurate DLPNO-CCSD(T) level⁵⁴ with the Def2-TZVP basis sets⁵⁵ and the Def2-TZVPP pseudopotential for La³⁴, utilizing the AutoAux generation procedure⁵⁵. We also used the 4f-in-core pseudopotential³⁴ for the simulation of the PE spectrum of $\text{Tb}_3\text{B}_{18}^-$ without consideration of the 4f electron detachment channels. Previous studies showed that such detachment channels carried very low detachment cross sections at the low detachment photon energies used and the main PES features of Ln–B binary clusters were dominated by MOs with Ln *sd* or B *sp* characters^{31–33}. Chemical bonding and electronic structure analyses were carried out by canonical molecular orbital (MO) theory and the semi-localized AdNDP method³⁹. We also performed calculations using the energy decomposition analysis–natural orbitals for chemical valence (EDA–NOCV) approach³⁸ to quantitatively elucidate the bonding mechanisms between the B_{18} and La_3^- moieties. The bond order indexes of different interatomic interactions were calculated using the Mayer⁵⁶, Gopinathan–Jug (G–J)⁵⁷, and Nalewajski–Mrozek schemes⁵⁸.

Data availability

The data that support the findings of this study are available within the article and the associated Supplementary information. Any other data are available from the corresponding authors upon request.

Code availability

The TGMIn code used for the global minimum search is available from the corresponding author (J.L.) upon request and signing a license.

Received: 14 January 2020; Accepted: 4 May 2020;

Published online: 02 June 2020

References

- Lipscomb, W. N. The boranes and their relatives. *Science* **196**, 1047–1055 (1977).
- Oganov, A. R. et al. Ionic high-pressure form of elemental boron. *Nature* **457**, 863–866 (2009).
- Albert, B. & Hillebrecht, H. Boron: elementary challenge for experimenters and theoreticians. *Angew. Chem. Int. Ed.* **48**, 8640–8668 (2009).
- Gindulytė, A., Lipscomb, W. N. & Massa, L. Proposed boron nanotubes. *Inorg. Chem.* **37**, 6544–6545 (1998).
- Boustani, I., Quandt, A., Hernández, E. & Rubio, A. New boron based nanostructured materials. *J. Chem. Phys.* **110**, 3176–3185 (1999).
- Tang, H. & Ismail-Beigi, S. Novel precursors for boron nanotubes: the competition of two-center and three-center bonding in boron sheets. *Phys. Rev. Lett.* **99**, 115501 (2007).
- Yang, X., Ding, Y. & Ni, J. Ab initio prediction of stable boron sheets and boron nanotubes: structure, stability, and electronic properties. *Phys. Rev. B* **77**, 041402 (2008).
- Zhai, H. J., Kiran, B., Li, J. & Wang, L. S. Hydrocarbon analogs of boron clusters: Planarity, aromaticity, and antiaromaticity. *Nat. Mater.* **2**, 827–833 (2003).
- Alexandrova, A. N., Boldyrev, A. I., Zhai, H. J. & Wang, L. S. All-boron aromatic clusters as potential new inorganic ligands and building blocks in chemistry. *Coord. Chem. Rev.* **250**, 2811–2866 (2006).
- Sergeeva, A. P. et al. Understanding boron through size-selected clusters: structure, chemical bonding, and fluxionality. *Acc. Chem. Res.* **47**, 1349–1358 (2014).
- Wang, L. S. Photoelectron spectroscopy of size-selected boron clusters: from planar structures to borophenes and borospherenes. *Int. Rev. Phys. Chem.* **35**, 69–142 (2016).
- Piazza, Z. A. et al. Planar hexagonal B_{36} as a potential basis for extended single-atom layer boron sheets. *Nat. Commun.* **5**, 3113 (2014).
- Mannix, A. J. et al. Synthesis of borophenes: anisotropic, two-dimensional boron polymorphs. *Science* **350**, 1513–1516 (2015).
- Feng, B. et al. Experimental realization of two-dimensional boron sheets. *Nat. Chem.* **8**, 563 (2016).
- Mannix, A. J., Zhang, Z., Guisinger, N. P., Yakobson, B. I. & Hersam, M. C. Borophene as a prototype for synthetic 2D materials development. *Nat. Nanotechnol.* **13**, 444 (2018).
- Zhai, H. J. et al. Observation of an all-boron fullerene. *Nat. Chem.* **6**, 727 (2014).
- Chen, Q. et al. Experimental and theoretical evidence of an axially chiral borospherene. *ACS Nano* **9**, 754–760 (2014).
- Lu, X., Feng, L., Akasaka, T. & Nagase, S. Current status and future developments of endohedral metallofullerenes. *Chem. Soc. Rev.* **41**, 7723–7760 (2012).
- Zhang, X. et al. A diuranium carbide cluster stabilized inside a C_{80} fullerene cage. *Nat. Commun.* **9**, 2753 (2018).
- Clemmer, D. E., Hunter, J. M., Shelimov, K. B. & Jarrold, M. F. Physical and chemical evidence for metallofullerenes with metal atoms as part of the cage. *Nature* **372**, 248–250 (1994).
- Branz, W. et al. Cage substitution in metal–fullerene clusters. *J. Chem. Phys.* **109**, 3425–3430 (1998).
- Vostrowsky, O. & Hirsch, A. Heterofullerenes. *Chem. Rev.* **106**, 5191–5207 (2006).
- Guo, B., Kerns, K. & Castleman, A. $\text{Ti}_8\text{C}_{12}^+$ -metallo-carbohedrenes: a new class of molecular clusters? *Science* **255**, 1411–1413 (1992).
- Dance, I. Ti_8C_{12} : barrierless transformation of the T_h Isomer to the T_d isomer. *J. Am. Chem. Soc.* **118**, 6309–6310 (1996).
- Romanescu, C., Galeev, T. R., Li, W. L., Boldyrev, A. I. & Wang, L. S. Aromatic metal-centered monocyclic boron rings: $\text{Co}@B_8^-$ and $\text{Ru}@B_9^-$. *Angew. Chem. Int. Ed.* **50**, 9334–9337 (2011).
- Romanescu, C., Galeev, T. R., Li, W. L., Boldyrev, A. I. & Wang, L. S. Transition-metal-centered monocyclic boron wheel clusters ($\text{M}@B_n^-$): a new class of aromatic borometallic compounds. *Acc. Chem. Res.* **46**, 350–358 (2012).
- Popov, I. A., Jian, T., Lopez, G. V., Boldyrev, A. I. & Wang, L. S. Cobalt-centred boron molecular drums with the highest coordination number in the CoB_{16}^- cluster. *Nat. Commun.* **6**, 8654 (2015).
- Li, W. L. et al. The planar CoB_{18}^- cluster as a motif for metallo-borophenes. *Angew. Chem. Int. Ed.* **55**, 7358–7363 (2016).
- Li, W. L. et al. From planar boron clusters to borophenes and metalloborophenes. *Nat. Rev. Chem.* **1**, 0071 (2017).
- Jian, T. et al. Probing the structures and bonding of size-selected boron and doped-boron clusters. *Chem. Soc. Rev.* **48**, 3550–3591 (2019).
- Li, W. L. et al. Observation of highly stable and symmetric lanthanide octa-boron inverse sandwich clusters. *Proc. Natl Acad. Sci. USA* **115**, E6972–E6977 (2018).
- Chen, T. T., Li, W. L., Li, J. & Wang, L. S. $[\eta\chi\text{-Bx}]\text{La}^-$ ($x = 7-9$): a new class of inverse sandwich complexes. *Chem. Sci.* **10**, 2534–2542 (2019).
- Chen, T. T., Li, W. L., Chen, W. J., Li, J. & Wang, L. S. $\text{La}_3\text{B}_{14}^-$: an inverse triple-decker lanthanide boron cluster. *Chem. Commun.* **55**, 7864–7867 (2019).
- Dolg, M., Stoll, H. & Preuss, H. A combination of quasi-relativistic pseudopotential and ligand field calculations for lanthanoid compounds. *Theor. Chim. Acta* **85**, 441–450 (1993).
- Malik, Z. P., Sologub, O., Grytsiv, A., Giester, G. & Rogl, P. F. Crystal structure of novel Ni–Zn borides: first observation of a boron–metal nested cage unit: B_{20}Ni_6 . *Inorg. Chem.* **50**, 7669–7675 (2011).
- Sergeeva, A. P., Averkiev, B. B., Zhai, H. J., Boldyrev, A. I. & Wang, L. S. All-boron analogues of aromatic hydrocarbons: B_{17}^- and B_{18}^- . *J. Chem. Phys.* **134**, 224304 (2011).
- Scheifers, J. P., Zhang, Y. & Fokwa, B. P. Boron: Enabling exciting metal-rich structures and magnetic properties. *Acc. Chem. Res.* **50**, 2317–2325 (2017).
- Mitoraj, M. P., Michalak, A. & Ziegler, T. A combined charge and energy decomposition scheme for bond analysis. *J. Chem. Theory Comput.* **5**, 962–975 (2009).
- Zubarev, D. Y. & Boldyrev, A. I. Developing paradigms of chemical bonding: adaptive natural density partitioning. *Phys. Chem. Chem. Phys.* **10**, 5207–5217 (2008).
- Schleyer, P. v. R., Maerker, C., Dransfeld, A., Jiao, H. & van Eikema Hommes, N. J. Nucleus-independent chemical shifts: a simple and efficient aromaticity probe. *J. Am. Chem. Soc.* **118**, 6317–6318 (1996).
- Cui, P. et al. A multicentre-bonded $[\text{Zn}^I]_8$ cluster with cubic aromaticity. *Nat. Commun.* **6**, 6331 (2015).

42. Bai, H. et al. Planar B_{41}^- and B_{42}^- clusters with double-hexagonal vacancies. *Nanoscale* **11**, 23286–23295 (2019).
43. Mbarki, M., St. Touzani, R. & Fokwa, B. P. Unexpected synergy between magnetic iron chains and stacked B_6 rings in $Nb_6Fe_{1-x}Ir_{6+x}B_8$. *Angew. Chem. Int. Ed.* **53**, 13174–13177 (2014).
44. Sharma, N., Zhang, Y., Fokwa, B., Mbarki, M. & Huq, A. Structural-distortion-driven magnetic transformation from ferro- to ferrimagnetic iron chains in B_6 -based $Nb_6FeIr_xB_8$. *Angew. Chem. Int. Ed.* **57**, 10323–10327 (2018).
45. Zhao, Y., Chen, X. & Li, J. TGMIn: a global-minimum structure search program based on a constrained basin-hopping algorithm. *Nano Res.* **10**, 3407–3420 (2017).
46. Perdew, J. P., Burke, K. & Ernzerhof, M. Generalized gradient approximation made simple. *Phys. Rev. Lett.* **77**, 3865–3868 (1996).
47. Van Lenthe, E. & Baerends, E. J. Optimized Slater-type basis sets for the elements 1–118. *J. Comput. Chem.* **24**, 1142–1156 (2003).
48. ADF, SCM, Theoretical Chemistry, Vrije Universiteit, (Amsterdam, The Netherlands, 2017). <http://www.scm.com>.
49. Lenthe, E. V., Baerends, E.-J. & Snijders, J. G. Relativistic regular two-component Hamiltonians. *J. Chem. Phys.* **99**, 4597–4610 (1993).
50. Adamo, C. & Barone, V. Toward reliable density functional methods without adjustable parameters: the PBE0 model. *J. Chem. Phys.* **110**, 6158–6170 (1999).
51. VandeVondele, J. et al. Quickstep: fast and accurate density functional calculations using a mixed Gaussian and plane waves approach. *Comput. Phys. Commun.* **167**, 103–128 (2005).
52. Li, J., Li, X., Zhai, H. J. & Wang, L. S. Au_{20} : a tetrahedral cluster. *Science* **299**, 864–867 (2003).
53. Schipper, P. R., Gritsenko, O. V., van Gisbergen, S. J. & Baerends, E. J. Molecular calculations of excitation energies and (hyper) polarizabilities with a statistical average of orbital model exchange-correlation potentials. *J. Chem. Phys.* **112**, 1344–1352 (2000).
54. Neese, F., Hansen, A. & Liakos, D. G. Efficient and accurate approximations to the local coupled cluster singles doubles method using a truncated pair natural orbital basis. *J. Chem. Phys.* **131**, 064103 (2009).
55. Weigend, F. & Ahlrichs, R. Balanced basis sets of split valence, triple zeta valence and quadruple zeta valence quality for H to Rn: design and assessment of accuracy. *Phys. Chem. Chem. Phys.* **7**, 3297–3305 (2005).
56. Mayer, I. Bond orders and valences from ab initio wave functions. *Int. J. Quantum Chem.* **29**, 477–483 (1986).
57. Gopinathan, M. & Jug, K. Valency. I. A quantum chemical definition and properties. *Theor. Chim. Acta* **63**, 497–509 (1983).
58. Michalak, A., DeKock, R. L. & Ziegler, T. Bond multiplicity in transition-metal complexes: applications of two-electron valence indices. *J. Phys. Chem. A* **112**, 7256–7263 (2008).

Acknowledgements

The experiment done at Brown University was supported by the National Science Foundation (CHE-1763380). The theoretical work done at Tsinghua University was

supported by the National Natural Science Foundation of China (21590792, 91426302, and 21433005). The calculations were done using supercomputers at the Southern University of Science and Technology (SUSTech), Tsinghua National Laboratory for Information Science and Technology, and the Computational Chemistry Laboratory of the Department of Chemistry under the Tsinghua Xuetang Talents Program.

Author contributions

T.-T.C. and W.-J.C. conducted the experiment; W.-L.L. did the calculations with assistance from X.-H.Y. and X.-R.D.; J.L. and L.-S.W. guided the work. T.-T.C., W.-L.L., J.L., and L.-S.W. co-wrote the manuscript. All the authors read and commented on the manuscript.

Competing interests

The authors declare no competing interests.

Additional information

Supplementary information is available for this paper at <https://doi.org/10.1038/s41467-020-16532-x>.

Correspondence and requests for materials should be addressed to W.-L.L., J.L. or L.-S.W.

Peer review information *Nature Communications* thanks Boniface Fokwa, Panagiotis Karamanis and the other, anonymous, reviewer(s) for their contribution to the peer review of this work.

Reprints and permission information is available at <http://www.nature.com/reprints>

Publisher's note Springer Nature remains neutral with regard to jurisdictional claims in published maps and institutional affiliations.



Open Access This article is licensed under a Creative Commons Attribution 4.0 International License, which permits use, sharing, adaptation, distribution and reproduction in any medium or format, as long as you give appropriate credit to the original author(s) and the source, provide a link to the Creative Commons license, and indicate if changes were made. The images or other third party material in this article are included in the article's Creative Commons license, unless indicated otherwise in a credit line to the material. If material is not included in the article's Creative Commons license and your intended use is not permitted by statutory regulation or exceeds the permitted use, you will need to obtain permission directly from the copyright holder. To view a copy of this license, visit <http://creativecommons.org/licenses/by/4.0/>.

© The Author(s) 2020